Astronomy & Astrophysics

^{26}Al kinematics: superbubbles following the spiral arms?

Constraints from the statistics of star clusters and HI supershells

Martin G. H. Krause[1,2,6], Roland Diehl[2,1], Yiannis Bagetakos[3,4], Elias Brinks[5], Andreas Burkert[6,1,2], Ortwin Gerhard[2], Jochen Greiner[2], Karsten Kretschmer[7], and Thomas Siegert[2]

[1] Excellence Cluster Universe, Technische Universität München, Boltzmannstrasse 2, 85748 Garching, Germany
e-mail: krause@mpe.mpg.de
[2] Max-Planck-Institut für extraterrestrische Physik, Giessenbachstr. 1, 85741 Garching, Germany
[3] Kapteyn Astronomical Institute, University of Groningen, Postbus 800, 9700 AV Groningen, The Netherlands
[4] Netherlands Institute for Radio Astronomy, Postbus 2, 7990 Dwingeloo, The Netherlands
[5] Centre for Astrophysics Research, University of Hertfordshire, Hatfield AL10 9AB, UK
[6] Universitäts-Sternwarte München, Ludwig-Maximilians-Universität, Scheinerstr. 1, 81679 München, Germany
[7] François Arago Centre, APC, Université Paris Diderot, CNRS/IN2P3, CEA/Irfu, Observatoire de Paris, Sorbonne Paris Cité, 10 rue Alice Domon et Léonie Duquet, 75205 Paris Cedex 13, France

ABSTRACT

Context. High-energy resolution spectroscopy of the 1.8 MeV radioactive decay line of ^{26}Al with the SPI instrument onboard the INTEGRAL satellite has recently revealed that diffuse ^{26}Al has higher velocities than other components of the interstellar medium in the Milky Way. ^{26}Al shows Galactic rotation in the same sense as the stars and other gas tracers, but reaches excess velocities of up to 300 km s^{-1}.

Aims. We investigate whether this result can be understood in the context of superbubbles, taking into account the statistics of young star clusters and HI supershells as well as the association of young star clusters with spiral arms.

Methods. We derived energy output and ^{26}Al mass of star clusters as a function of the cluster mass by population synthesis from stellar evolutionary tracks of massive stars. Using the limiting cases of weakly and strongly dissipative superbubble expansion, we linked this to the size distribution of HI supershells and assessed the properties of possible ^{26}Al-carrying superbubbles.

Results. ^{26}Al is produced by star clusters of all masses above $\approx 200\,M_\odot$, is roughly equally contributed over a logarithmic star cluster mass scale and strongly linked to the injection of feedback energy. The observed superbubble size distribution cannot be related to the star cluster mass function in a straightforward manner. To avoid the added volume of all superbubbles exceeding the volume of the Milky Way, individual superbubbles have to merge frequently. If any two superbubbles merge, or if ^{26}Al is injected off-centre into a larger HI supershell, we expect the hot ^{26}Al-carrying gas to obtain velocities of the order of the typical sound speed in superbubbles, ≈ 300 km s^{-1} before decay. For star formation coordinated by the spiral arm pattern which, inside co-rotation, is overtaken by the faster moving stars and gas, outflows from spiral arm star clusters would preferentially flow into the cavities that are inflated by previous star formation associated with this arm. These cavities would preferentially be located towards the leading edge of a given arm.

Conclusions. This scenario might explain the ^{26}Al kinematics. The massive-star ejecta are expected to survive $\geq 10^6$ yr before being recycled into next-generation stars.

Key words. gamma rays: ISM – ISM: kinematics and dynamics – ISM: bubbles – ISM: structure – Galaxy: structure

1. Introduction

The possibilities of obtaining kinematic information for the hot phase of the interstellar medium (ISM) are generally very limited. While multimillion-degree gas is common and metal lines are observed (e.g., Henley & Shelton 2012), the spectral resolution typically does not allow constraining flows of hot gas in galaxy clusters in a meaningful way (Biffi et al. 2013), even more so for the lower velocities in the ISM.

The gamma-ray spectrometer onboard INTEGRAL (SPI, Vedrenne et al. 2003; Winkler et al. 2003) has a spectral resolution of ≈ 3 keV at 1.8 MeV, where ^{26}Al can be observed through its characteristic γ-ray decay line. With increasing exposure times (Diehl et al. 2006; Kretschmer et al. 2013, Paper I in the following), it has become possible to measure the centroid position of the line with an accuracy of tens of km s^{-1}, sufficient to clearly observe the Doppler shift due to large-scale rotation along the ridge of the Galaxy within longitudes $|l| < 35$ deg.

Toward the Galactic centre ($l = 0$), the apparent ^{26}Al velocity is zero with a hint for a weak blueshift. For greater positive (negative) longitudes, the projected velocity rises beyond 200 (-200) km s^{-1}. The direction of the line shift corresponds to Galactic rotation, but its magnitude is significantly larger than that expected from CO and HI. Paper I also showed that an ad hoc model assuming forward blowout at 200 km s^{-1} from the spiral arms of the inner Galaxy can explain the data well. The physical interpretation would be that ^{26}Al is ejected into the hot phase of the ISM in superbubbles at the leading edges of the gaseous spiral arms. Hydrodynamic interaction with the locally anisotropic ISM would then lead to a preferential expansion of the superbubbles into the direction of Galactic rotation (in addition to out-of-plane blowout).

The sources of diffuse, interstellar ^{26}Al are massive star winds and supernovae (Prantzos & Diehl 1996). These are energetic events, which lead to the formation of bubbles (one massive star) and, because massive stars often occur together with other

massive stars in associations and bound clusters (e.g., Zinnecker & Yorke 2007; Kroupa et al. 2013; Krumholz 2014), superbubbles. Superbubbles are observed in many different wavelengths (e.g., Krause et al. 2014). Statistical information is, however, mainly restricted to sizes and kinematics of the cavities seen in HI. Bagetakos et al. (2011) analyzed 20 nearby spiral galaxies, whose properties are thought to be similar to those of the Milky Way, and found more than 1000 HI holes. We use their data as reference below. Oey & Clarke (1997) have connected the statistics of HI holes to the star cluster mass function, finding that the sizes and velocities of HI holes may be explained by massive star activity in star clusters (compare below, however). Because this association is established now, we use the term HI supershells instead of HI holes for clarity throughout.

The ^{26}Al measurement constitutes another piece of statistical information for bubbles and superbubbles. ^{26}Al decays on a timescale of 1 Myr, much shorter than typical superbubble lifetimes (e.g., Oey & García-Segura 2004; Bagetakos et al. 2011; Heesen et al. 2015). Hence, we may expect it to reflect internal dynamics.

Here, we connect the observed ^{26}Al kinematics to the statistics of star clusters (Sect. 2) and superbubbles (HI supershells, Sect. 3) to better understand the large-scale gas flows traced by ^{26}Al. In particular, we are interested in constraining superbubble merging, because superbubble merging may lead to asymmetric motions relative to the parent star clusters, when gas from a high-pressure superbubble streams into a low-pressure cavity. We find that star clusters of all masses contribute to the ^{26}Al signal. Oey & Clarke (1997) investigated superbubble merging in the Milky Way with inconclusive results. With updated models and a newly derived star formation rate, we find frequent merging. Hence, we expect the ^{26}Al-traced hot outflows to be injected into pre-existing superbubbles. We then argue in Sect. 4 that the spatial co-ordination of star formation in the Milky Way by the spiral arms may lead to the observed ^{26}Al kinematics.

2. Which star clusters produce how much ^{26}Al?

Star formation generally takes place in clusters and associations, the majority of which disperse after some time (Lada & Lada 2003; Kruijssen 2012). It is debated for bound star clusters whether the dispersal is due to gas expulsion (e.g., Gieles & Bastian 2008). Recent observations did not find the expansion velocities that are expected if gas expulsion was important (e.g., Hénault-Brunet et al. 2012). Hence, the dispersal is probably related to tidal effects (e.g., Kruijssen et al. 2012a) that could take as long as 200 Myr (Kruijssen et al. 2012b). It is therefore reasonable to assume that for the timescales of interest here, the great majority of massive stars are grouped (compare also Zinnecker & Yorke 2007). The mass function of embedded star clusters (mostly unbound), which is where most star formation takes place locally (Lada & Lada 2003), has a slope very similar to that of star clusters in external galaxies (compare below). Therefore, we assume just one mass function for star-forming regions in the following and generally use the term star cluster without a qualifying adjective to subsume bound and unbound star-forming regions.

For spiral galaxies like the Milky Way, the initial cluster mass function (ICMF) is given by (e.g., Larsen 2009; Bastian et al. 2012)

$$\frac{\mathrm{d}N}{\mathrm{d}M} = a \left(M/M_\mathrm{c}\right)^{\alpha} \exp\left(-M/M_\mathrm{c}\right), \tag{1}$$

where a is the normalisation, the cutoff mass $M_\mathrm{c} = 2 \times 10^5 \, M_\odot$, and we take the power-law index α to be -2; compare also the

reviews by Lada & Lada (2003), Kroupa et al. (2013), Krumholz (2014). Following Lada & Lada (2003), we adopted a lower limit for star cluster masses of 50 $M_\odot$. Embedded star clusters have not been shown to possess an exponential cutoff. We therefore checked that the presence of the high-mass cutoff only marginally influences our results.

Since only massive stars produce ^{26}Al, we have to relate the occurrence of massive stars to the masses of star clusters. We carried out the entire analysis for both optimal sampling (Kroupa et al. 2013), where the masses of massive stars are fixed for a given star cluster mass, and random sampling (e.g., Krumholz 2014). For random sampling, we fixed the stellar mass above 6 $M_\odot$ to the corresponding fraction of the initial mass function (IMF) from Kroupa et al. (2013). While the extreme assumption of optimal sampling has recently been challenged (Andrews et al. 2014), we use it here to demonstrate that even such a strong truncation of the IMFs would not affect the conclusions.

For these groups of massive stars, we used the population synthesis results from Voss et al. (2009; stellar evolutionary tracks of rotating stars of Meynet & Maeder 2005 and wind velocities from Lamers et al. 1995 and Niedzielski & Skorzynski 2002 for the Wolf-Rayet phase) to obtain the ^{26}Al mass as well as the energy injected into the ISM by massive stars as a function of time and stellar mass. The release of mass, energy, and ^{26}Al is largely completed after about 48 Myr, the lifetime of stars of about 8 $M_\odot$, also broadly consistent with the age estimates for HI supershells given by Bagetakos et al. (2011). Not all the stars in a cluster might form at the same time. However, typical age spreads within clusters are of the order of 1 Myr or less (e.g., Niederhofer et al. 2015), which is much shorter than the timescales of interest. We therefore used the star cluster population up to 48 Myr for our model. Following Chomiuk & Povich (2011), we took 1.9 $M_\odot$ yr^{-1} for the star formation rate of the Milky Way. This sets the constant in Eq. (1) to $a = 3\times10^{-4} \, M_\odot^{-1}$. Uncertainties in this parameter are substantial (compare also Kennicutt & Evans 2012).

With these assumptions, we calculated the time-averaged ^{26}Al mass for a given star cluster. For each star cluster, we first determined the masses of its stars above 8 $M_\odot$ by the optimal sampling method, the amount of released ^{26}Al from Voss et al. (2009), taking into account radioactive decay, and finally averaged over time (48 Myr). The result is shown in Fig. 1. Apart from small features towards lower masses, the ^{26}Al yield is almost linear even for optimal sampling. For star clusters below about 1000 $M_\odot$, the sampling method matters. For both random and optimal sampling, the ^{26}Al mass per cluster drops below the linear relation because the IMF can no longer be fully sampled (e.g., a 120 $M_\odot$ star may not live in a 50 $M_\odot$ star cluster). We note that using the IMF directly to predict the Galactic ^{26}Al mass, that is, without dividing the mass of young stars into star clusters, yields a value higher by about 20 per cent.

The ICMF has roughly equal mass in each decade of star cluster mass (within the cutoffs). This remains true with the ^{26}Al mass folded in because the latter is roughly proportional to the star cluster mass: star clusters of each decade in mass, from a few hundred to about 10^5 $M_\odot$, contribute about equally to the observed ^{26}Al signal (Fig. 1).

3. Superbubble size distributions and merging

Here, we investigated whether merging of superbubbles is common in the Milky Way. We followed the overall procedure described in Oey & Clarke (1997), but updated the expansion models from our own 3D hydrodynamics simulation studies
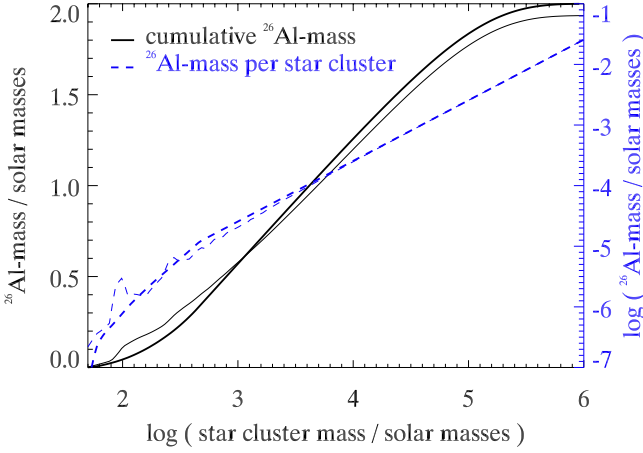
Fig. 1. ^{26}Al mass for individual star clusters of given mass (dotted blue, right vertical scale) and cumulative ^{26}Al mass for the Milky Way as a function of star cluster mass, assuming a star formation rate of 1.9 $M_\odot$ yr^{-1} (solid black, left vertical scale). Thin (thick) lines are for the case of truncated IMFs (random sampling). In the limit of high star cluster masses, 2.6×10^{-8} $M_\odot$ of ^{26}Al is produced per unit stellar mass formed. The blue dashed curves are therefore linear, down to about 1000 $M_\odot$, where sampling effects become important.

(compare below). While towards the low-mass end, the ICMF includes many objects with only one massive star, which will produce a single-star bubble, we use the term superbubble below for simplicity for all bubbles produced by the star clusters.

Mac Low & McCray (1988) presented a self-similar model for superbubble expansion, where the superbubble expands steadily with the radius r proportional to a power law in time t. About 35 per cent of the injected energy, $E(t)$, is dissipated radiatively in this model. This model should be increasingly adequate for larger superbubbles, with more frequent explosions, and at later times.

In Krause et al. (2013) and Krause & Diehl (2014), we have developed a more strongly dissipative model from 3D hydrodynamics simulations. The reason for the stronger dissipation is the more realistic, non-steady energy input and the emergence of a highly radiative mixing layer due to 3D instabilities. Our results are well approximated by 90 per cent dissipation in the steady energy input phase before the first supernova and a decline of the current energy, $E(t)$, after each supernova with time t as $t^{-3/4}$ (momentum-conserving snowplough). Both are an upper limit on the energy dissipation because we still observed a slight dependence on numerical resolution in the pre-supernova phase ($\approx$88 per cent dissipation at the highest resolution), and, as the superbubble expands, the density around star clusters will drop below the 10 cm^{-3} we assumed in the simulations. The strongly dissipative model should be more adequate for superbubbles with few supernovae, and indeed explains the X-ray-luminosity-kinematics relation well, for instance (Krause & Diehl 2014).

We used the evolution of the superbubble energy $E(t)$ from both models and predict the radius in the thin shell approximation following Krause & Diehl (2014). Their Eq. (3) for constant ambient density ρ_0 evaluates to $r^5 = 15/(2\pi\rho_0) \int_0^t dt' \int_0^{t'} dt'' E(t'')$.

We calculated models for both random and optimal sampling. For the weakly dissipative models, we also added models for which we took a constant ISM pressure of $P_0 = 3800 k_B$K cm^{-3} (Jenkins & Tripp 2011) into account, which limits the expansion. The momentum equation may then be written

as (Krause 2005) $\partial^2 Y(r)/\partial t^2 = E(t) - 2\pi r^3 P_0$, with $Y(r) = 2\pi\rho_0 r^5/15$, which we solved numerically. For this model, we also regarded a superbubble as dissolved when the expansion velocity had dropped to 10 km s^{-1} and perturbations with this velocity had time to grow to the size of the superbubble, similar to the stalled-and-surviving mode in Oey & Clarke (1997). We did not investigate this option for the strong dissipation models because the assumption of momentum conservation after each supernova explosion implies a total pressure force of zero.

For the following analysis, we neglected the shear gradient from Galactic rotation. It is typically 10−50 km s^{-1} kpc^{-1} (Bagetakos et al. 2011) and therefore has a small effect on active superbubbles, in agreement with the moderate asymmetries found by Bagetakos et al. (2011), but will eventually destroy old superbubbles. The finite exponential scaleheight H of the ISM introduces a cutoff in the superbubble radii in the Galactic plane due to blow-out-related pressure loss at $\approx$3H (Baumgartner & Breitschwerdt 2013). We set this cutoff superbubble radius to 1 kpc for the whole sample and to 0.5 kpc for the Milky Way modelling below because of the lower HI scaleheight (Narayan & Jog 2002; Langer et al. 2014).

We first calculated the fractional distributions of superbubble diameters for three different assumptions for the background density for the sample of star-forming galaxies from Bagetakos et al. (2011), that is, $H = 1/3$ kpc, and compared this to the observations in Fig. 2. Generally, models with a lower background density provide a better match to the observations. As expected, the weakly dissipative model more closely represents the large superbubbles. The model is not quite satisfactory because the density required to reach the larger diameters, 0.1 cm^{-3}, is on the low side of values suggested by observations, 0.1−0.7 cm^{-3} (Bagetakos et al. 2011). One might be able to interpret this finding by shear effects, adopting a higher density, that is, choosing a curve between the dotted blue and solid black lines in Fig. 2.

The strongly dissipative models may produce a significant population at around 1 kpc diameter, but, on the other hand, cannot account for large HI supershells. ISM pressure is strongest for intermediate-size HI supershells and for low ISM density ($\approx$1 kpc for $\rho_0 = 0.1$ cm^{-3}). At high ISM densities, ISM pressure is negligible, but in these models many slower and smaller superbubbles are destroyed when considering ISM turbulence, which increases the fraction of larger superbubbles. The IMF sampling method has a minor effect on the results (compare Fig. 2).

We can now predict the superbubble distribution for the Milky Way from the star formation rate using the procedure outlined above, now with $H = 1/6$ kpc. The fractional distributions are identical to Fig. 2, but cut at 1 kpc due to the reduced scale height. The observed fractional HI supershell diameter distribution for the Milky Way (Ehlerová & Palouš 2013) is consistent with the distribution of external star-forming galaxies from (Bagetakos et al. 2011), which we used here.

Because for the Milky Way the total number of superbubbles is constrained by the star-formation rate, we may now check for superbubble merging by calculating the total volume predicted by our model to be occupied by superbubbles and comparing it to the volume of the Milky Way ISM. The total occupied volume for the given star formation rate exceeds the volume of the Milky Way ISM (cylinder: 10 kpc radius, 1 kpc thickness) for all assumptions (Table 1).

This indicates that the superbubbles merge frequently. The volume of merging superbubbles is not simply the sum of the individual volumes, but is much smaller. The observed volume fractions of HI supershells (3D porosity) are typically below 10 per cent and may reach 20 per cent in later Hubble types
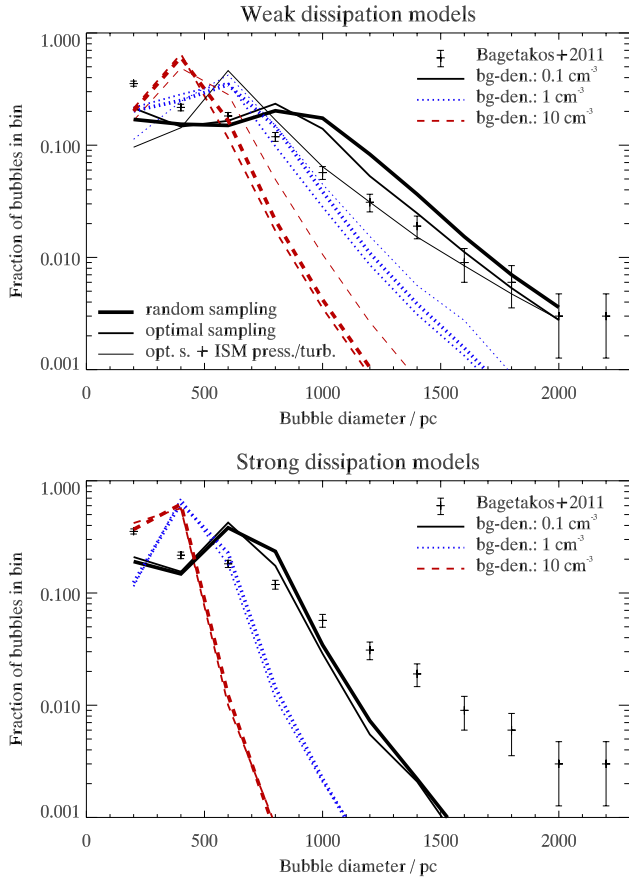
Fig. 2. Superbubble diameter distributions for the weakly (*top*) and the strongly (*bottom*) dissipative model for three different choices of the background density (bg den. in the legends). The size of the bins is 200 pc. Thick lines are for random sampling, thinner lines for optimal sampling, and the thinnest lines in the *top panel* are for optimal sampling where the background pressure and superbubble destruction by ISM turbulence are taken into account. The minimum near 400 pc for the solid curves is due to the strong acceleration after the first supernova in a superbubble. It is below the data range for the other curves. Large superbubbles are better explained by the weakly dissipative model.

Table 1. Galaxy-integrated superbubble volumes in units of the Milky Way volume, assuming a maximum superbubble diameter of 1 kpc due to blowout.

Dissipation	$\rho_0 = 0.1$ cm^{-3}	$\rho_0 = 1$ cm^{-3}	$\rho_0 = 10$ cm^{-3}
weak	115/115/33	40/38/22	11/11/6.1
strong	47/49	12/13	3.1/3.3

Notes. For each entry, the first (second) number is for random sampling (truncated IMFs). For weak-dissipation models, we also give the numbers for the models that take into account the ISM background pressure and turbulence as the third number.
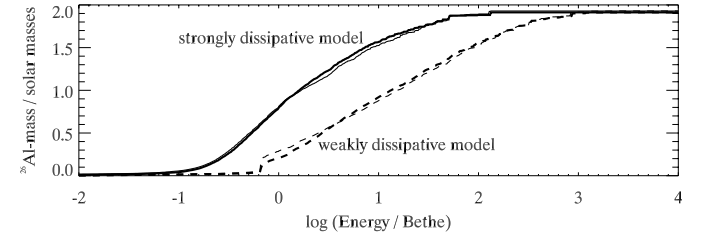
Fig. 3. Cumulative ^{26}Al mass over current superbubble energy for weakly (dotted) and strongly (solid) dissipative models for a star cluster population representative of the Milky Way. 1 Bethe = 10^{51} erg.

parts, and the shell around Upper Scorpius is half merged into an older supershell. The whole structure is expected to merge within a few Myr with the Local Bubble (Breitschwerdt & de Avillez 2006). Evidence for superbubble merging from extragalactic studies is scarce, however, probably because of the low resolution (typically around 200 pc). Hα bubbles are found at the rims of HI supershells, however (Egorov et al. 2014).

Superbubble merging may produce significant net velocities in ejecta flows with respect to the driving massive-star group. Because the ^{26}Al content is correlated with the energy content of a superbubble (Fig. 3), we expect overpressured ^{26}Al-rich material to often stream into superbubbles with lower pressure once the interface is eroded. The situation is similar when the ^{26}Al production site is located towards one end of an already merged larger superbubble.

4. Model for the ^{26}Al kinematics

In the preceding sections, we have demonstrated that star clusters of all masses are equally important as ^{26}Al producers, and that, on Galactic scales, star clusters cannot be assigned to individual superbubbles because of frequent superbubble merging. Our model also shows that ^{26}Al injection from star clusters is strongly correlated to energy injection (Fig. 3). It follows that ^{26}Al is probably observed in motion, and in particular, it probably traces gas involved in superbubble merging. Based on these findings, we suggest the following model (Fig. 4) to explain the ^{26}Al kinematics.

When spiral arms sweep through the Galactic disc, they trigger the formation of young star clusters that produce large superbubbles, which are traced as HI supershells. During the observed lifetimes of HI supershells, ≲100 Myr (Bagetakos et al. 2011), a spiral arm may lag behind stars and gas by as much as a few kpc as a result of the pattern speed of the arm, which is lower within co-rotation than the rotational speed of the stars and gas. The current young star clusters in a spiral arm therefore feed ^{26}Al-carrying ejecta into the HI supershells left behind by the receding spiral arm (sketch in Fig. 4).
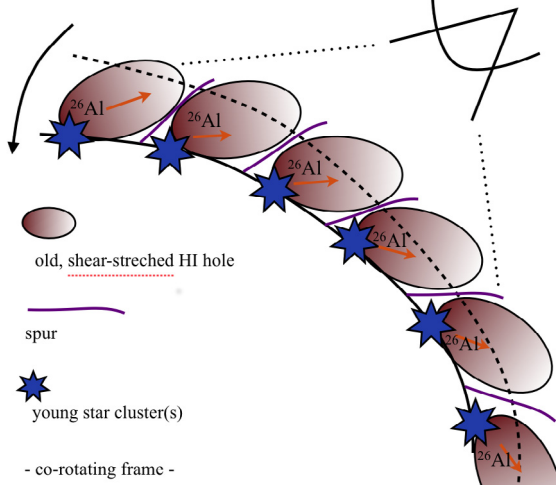
(Bagetakos et al. 2011). A superbubble volume fraction of about 20 per cent is expected from the hot-gas fraction in the ISM simulations of de Avillez & Breitschwerdt (2005). Combined with our analysis, this strengthens the point about superbubble merging. A consistent interpretation would be that the smaller superbubbles in the diameter distribution (Fig. 2) merge to obtain more HI supershells at large diameters. This would also alleviate the requirement for low ambient density (compare above).

There is much direct evidence for superbubble merging in the Milky Way: 29 per cent of the bubbles identified in The Milky Way Project, a citizen-science project that identified 5106 bubbles in the Milky Way (many of which are single-star bubbles), showed signs of merging (Simpson et al. 2012). Often, secondary bubbles are found at the edge of larger bubbles. Ehlerová & Palouš (2013) calculated the porosity for the Milky Way as a function of radius from 333 identified HI supershells. They found porosities higher than unity inside of the solar circle, and thus strong overlap of superbubbles. The closest massive star group, Scorpius-Centaurus OB2, is an excellent example for superbubble merging (Pöppel et al. 2010; Preibisch & Mamajek 2008): the different subgroups of the OB association appear to have been triggered by expanding shells from the older
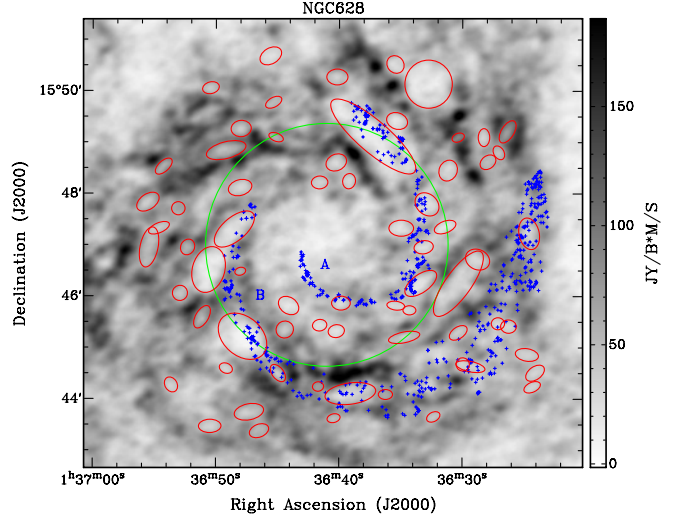
Fig. 4. Sketch of the proposed model for explaining the ^{26}Al kinematics. In the co-rotating frame chosen here, a spiral arm (solid line) moves anti-clockwise. At its previous location (dashed line), it created large superbubbles (ellipses), blowing out of the disc. The young star clusters (blue stars) at the current spiral arm location feed ^{26}Al (colour gradient in ellipses) into the old superbubbles.

Fig. 5. Grand-design spiral galaxy NGC 628. The background image is the 21 cm map from The HI Nearby Galaxy Survey (THINGS, Walter et al. 2008). Red ellipses denote HI supershells from Bagetakos et al. (2011). Blue plus-signs denote the 650 HII regions identified by Honig & Reid (2015). Their spiral arm designations, A and B, are also indicated. The large green circle indicates the median co-rotation radius of 4.6 ± 1.2 kpc from a number of studies as compiled by Scarano & Lépine (2013). For the first half-turn, arm A has no HI supershell on its trailing edge, but four are close to or even overlap the leading edge in the way envisaged by our model. Arm B begins just inside of co-rotation and has three prominent HI supershells at its leading edge, with only a minor one towards the trailing edge. From about the co-rotation radius outwards, HI supershells are no longer at the edges of the HII arm, but appear all over it.

Despite uncertainties regarding wind clumping (e.g., Bestenlehner et al. 2014) and dust production and clumping (e.g., Indebetouw et al. 2014; Williams 2014), the bulk of ^{26}Al is probably mixed into the diffuse gaseous ejecta that are expelled into the hot immediate surroundings of the stars. The ejecta do not keep their initial velocity ($\approx$1000 km s^{-1}) for long: for supernovae, they are shocked on timescales of 10^3 yr (Tenorio-Tagle et al. 1990). For Wolf-Rayet winds inside superbubbles, the free expansion phase can be up to 10^4 yr, or $\approx$10 pc (Krause et al. 2013). The ejecta then travel at a reasonable fraction of the sound speed in superbubbles, $c_s = \sqrt{1.62kT/m_p} = 279\, T_{0.5}^{1/2}$ km s^{-1}. Here, k is Boltzmann's constant, m_p the proton mass, T ($T_{0.5}$) the temperature (in units of 0.5 keV), and the numerical factor is calculated for a fully ionised plasma of 90 per cent hydrogen and 10 per cent helium by volume. Measurements of superbubble temperatures range from 0.1 keV to about 1 keV (e.g., Dunne et al. 2001; Jaskot et al. 2011; Sasaki et al. 2011; Kavanagh et al. 2012; Warth et al. 2014), in good agreement with expectations, if instabilities and mixing are taken into account (Krause et al. 2014).

In simulations of merging bubbles (Krause et al. 2013), we find such kinematics for gas flooding the cavities at lower pressure shortly after merging. The ejecta travel about 300 pc during one decay time (τ = 1 Myr), which corresponds to the size of the smaller HI supershells (Fig. 2), that is, the decay is expected to occur during the first crossing of the HI supershell.

Hence, we expect a one-sided ^{26}Al outflow at the superbubble sound speed, $\approx$300 km s^{-1}, in excellent agreement with the observations and their analysis presented in Paper I.

This model predicts a change in relative outflow direction near the co-rotation radius. But co-rotation in the Galaxy is unfortunately too far out (8.4−12 kpc, e.g., Martínez-Barbosa et al. 2015) to check for direction reversals in the data set of Paper I. At such galactocentric distances, individual ^{26}Al-emission regions are only a few, they are faint, and they are not associated with spiral arms. Thus, we do not expect large ^{26}Al velocity asymmetries, in good agreement with the measurements in Cygnus (Martin et al. 2009) and Scorpius-Centaurus (Diehl et al. 2010).

We might, however, expect to find HI supershells associated with the leading edge of spiral-arm star formation regions in nearby face-on spiral galaxies, inside their co-rotation radii. We investigated this for a few objects by combining HII regions from Honig & Reid (2015) with HI images with HI supershells using co-rotation radii from Tamburro et al. (2008) and Scarano & Lépine (2013). For NGC 3184 and NGC 5194 we found evidence for HI supershells close to HII regions in the spiral arms. There is no clear trend where the HI supershells are located with respect to the HII regions in NGC 5194, whereas more supershells appear on the trailing edge for NGC 3184.

In the case of NGC 628 (Fig. 5), Honig & Reid (2015) map HII regions for two arms, A and B, and inside co-rotation, HI supershells are indeed found close to and overlapping with the HII regions, preferentially at their leading edges. Especially for arm B, which is located in an HI – rich part of the galaxy, the HI supershell locations relative to the HII regions change strikingly near the co-rotation radius: inside, three prominent HI supershells lie towards the leading edge of the HII arm, extending over about a quarter of a turn. Only one small supershell is located at the trailing edge. From about the co-rotation radius outwards, the HI supershells are spread over the widening HII arm. None is clearly associated with the leading or trailing edges. It is beyond the scope of this article to explain the differences between these galaxies. The fact that the effect we postulate is consistent with the data in NGC 628 is encouraging, however.

The ^{26}Al decay time is similar to the crossing time through the HI supershell, and thus we expect to observe it while it crosses the HI supershells. A few Myr later, ^{26}Al should isotropise, advect vertically into the halo (e.g., de Avillez & Breitschwerdt 2005), or mix as a result of interaction with the

cavity walls. Most of the ^{26}Al has then decayed, and the contribution to the observed γ-ray signal is small.

5. Conclusions

We interpreted the observed ^{26}Al kinematics in the Galaxy as a consequence of superbubble formation propagating with the spiral arms and merging of young superbubbles into older HI supershells, with outflows from currently star-forming regions into the pre-shaped cavities from preceding star formation towards the leading edges of spiral arms.

The model does not rely on independent offsets between young stars and gaseous spiral arms, which might be created by other – not feedback-related – processes and which are a matter of ongoing research (compare, e.g., the review by Dobbs & Baba 2014).

We conclude that ^{26}Al mainly decays during the first crossing of superbubbles while in the hot phase. The bulk of ^{26}Al is therefore not mixing with cold gas on its decay timescale. ^{26}Al has been found in meteorites, however, indicating its presence in the gas that formed the Sun (e.g., Gounelle & Meynet 2012). The corresponding fraction of ^{26}Al required to mix into a star-forming cloud during the decay timescale is small, however (Vasileiadis et al. 2013), and would hardly affect our model.

References

Andrews, J. E., Calzetti, D., Chandar, R., et al. 2014, ApJ, 793, 4
Bagetakos, I., Brinks, E., Walter, F., et al. 2011, AJ, 141, 23
Bastian, N., Konstantopoulos, I. S., Trancho, G., et al. 2012, A&A, 541, A25
Baumgartner, V., & Breitschwerdt, D. 2013, A&A, 557, A140
Bestenlehner, J. M., Gräfener, G., Vink, J. S., et al. 2014, A&A, 570, A38
Biffi, V., Dolag, K., & Böhringer, H. 2013, MNRAS, 428, 1395
Breitschwerdt, D., & de Avillez, M. A. 2006, A&A, 452, L1
Chomiuk, L., & Povich, M. S. 2011, AJ, 142, 197
de Avillez, M. A., & Breitschwerdt, D. 2005, A&A, 436, 585
Diehl, R., Halloin, H., Kretschmer, K., et al. 2006, Nature, 439, 45
Diehl, R., Lang, M. G., Martin, P., et al. 2010, A&A, 522, A51
Dobbs, C., & Baba, J. 2014, PASA, 31, 35
Dunne, B. C., Points, S. D., & Chu, Y.-H. 2001, ApJS, 136, 119
Egorov, O. V., Lozinskaya, T. A., Moiseev, A. V., & Smirnov-Pinchukov, G. V. 2014, MNRAS, 444, 376
Ehlerová, S., & Palouš, J. 2013, A&A, 550, A23
Gieles, M., & Bastian, N. 2008, A&A, 482, 165
Gounelle, M., & Meynet, G. 2012, A&A, 545, A4
Heesen, V., Brinks, E., Krause, M. G. H., et al. 2015, MNRAS, 447, L1
Hénault-Brunet, V., Evans, C. J., Sana, H., et al. 2012, A&A, 546, A73
Henley, D. B., & Shelton, R. L. 2012, ApJS, 202, 14
Honig, Z. N., & Reid, M. J. 2015, ApJ, 800, 53
Indebetouw, R., Matsuura, M., Dwek, E., et al. 2014, ApJ, 782, L2
Jaskot, A. E., Strickland, D. K., Oey, M. S., Chu, Y.-H., & García-Segura, G. 2011, ApJ, 729, 28
Jenkins, E. B., & Tripp, T. M. 2011, ApJ, 734, 65
Kavanagh, P. J., Sasaki, M., & Points, S. D. 2012, A&A, 547, A19
Kennicutt, R. C., & Evans, N. J. 2012, ARA&A, 50, 531
Krause, M. 2005, A&A, 431, 45
Krause, M. G. H., & Diehl, R. 2014, ApJ, 794, L21
Krause, M., Fierlinger, K., Diehl, R., et al. 2013, A&A, 550, A49
Krause, M., Diehl, R., Böhringer, H., Freyberg, M., & Lubos, D. 2014, A&A, 566, A94
Kretschmer, K., Diehl, R., Krause, M., et al. 2013, A&A, 559, A99
Kroupa, P., Weidner, C., Pflamm-Altenburg, J., et al. 2013, in Planets, Stars and Stellar Systems, eds. T. Oswalt, & G. Gilmore (Springer Netherlands), 115
Kruijssen, J. M. D. 2012, MNRAS, 426, 3008
Kruijssen, J. M. D., Maschberger, T., Moeckel, N., et al. 2012a, MNRAS, 419, 841
Kruijssen, J. M. D., Pelupessy, F. I., Lamers, H. J. G. L. M., et al. 2012b, MNRAS, 421, 1927
Krumholz, M. R. 2014, Phys. Rep., 539, 49
Lada, C. J., & Lada, E. A. 2003, ARA&A, 41, 57
Lamers, H. J. G. L. M., Snow, T. P., & Lindholm, D. M. 1995, ApJ, 455, 269
Langer, W. D., Pineda, J. L., & Velusamy, T. 2014, A&A, 564, A101
Larsen, S. S. 2009, A&A, 494, 539
Mac Low, M.-M., & McCray, R. 1988, ApJ, 324, 776
Martin, P., Knödlseder, J., Diehl, R., & Meynet, G. 2009, A&A, 506, 703
Martínez-Barbosa, C. A., Brown, A. G. A., & Portegies Zwart, S. 2015, MNRAS, 446, 823
Meynet, G., & Maeder, A. 2005, A&A, 429, 581
Narayan, C. A., & Jog, C. J. 2002, A&A, 394, 89
Niederhofer, F., Hilker, M., Bastian, N., & Silva-Villa, E. 2015, A&A, 575, A62
Niedzielski, A., & Skorzynski, W. 2002, Acta Astron., 52, 81
Oey, M. S., & Clarke, C. J. 1997, MNRAS, 289, 570
Oey, M. S., & García-Segura, G. 2004, ApJ, 613, 302
Pöppel, W. G. L., Bajaja, E., Arnal, E. M., & Morras, R. 2010, A&A, 512, A83
Prantzos, N., & Diehl, R. 1996, Phys. Rep., 267, 1
Preibisch, T., & Mamajek, E. 2008, The Nearest OB Association: Scorpius-Centaurus (Sco OB2), ed. B. Reipurth, 235
Sasaki, M., Breitschwerdt, D., Baumgartner, V., & Haberl, F. 2011, A&A, 528, A136
Scarano, S., & Lépine, J. R. D. 2013, MNRAS, 428, 625
Simpson, R. J., Povich, M. S., Kendrew, S., et al. 2012, MNRAS, 424, 2442
Tamburro, D., Rix, H.-W., Walter, F., et al. 2008, AJ, 136, 2872
Tenorio-Tagle, G., Bodenheimer, P., Franco, J., & Rozyczka, M. 1990, MNRAS, 244, 563
Vasileiadis, A., Nordlund, Å., & Bizzarro, M. 2013, ApJ, 769, L8
Vedrenne, G., Roques, J.-P., Schönfelder, V., et al. 2003, A&A, 411, L63
Voss, R., Diehl, R., Hartmann, D. H., et al. 2009, A&A, 504, 531
Walter, F., Brinks, E., de Blok, W. J. G., et al. 2008, AJ, 136, 2563
Warth, G., Sasaki, M., Kavanagh, P. J., et al. 2014, A&A, 567, A136
Williams, P. M. 2014, MNRAS, 445, 1253
Winkler, C., Courvoisier, T. J.-L., Di Cocco, G., et al. 2003, A&A, 411, L1
Zinnecker, H., & Yorke, H. W. 2007, ARA&A, 45, 481